




Monte Carlo simulations of cold neutron spectra for various para- and ortho-hydrogen ratios using different codes and nuclear data libraries

Norberto Sebastián Schmidt^{1,a} , Alexander Schwab^{1,b}, Jingjing Li^{1,c}, Ulrich Rücker^{1,d}, Paul Zakalek^{1,e}, Eric Mauerhofer^{1,f}, Javier Dawidowski^{2,3,4,g}, Thomas Gutberlet^{1,h}

¹ Jülich Centre for Neutron Science, Forschungszentrum Jülich GmbH, Jülich 52425, North Rhine-Westphalia, Germany

² Instituto Balseiro, Universidad Nacional de Cuyo, Av. Bustillo 9500, San Carlos de Bariloche 8400, Río Negro, Argentina

³ Neutron Physics Department, Comisión Nacional de Energía Atómica (CNEA), Av. Bustillo 9500, San Carlos de Bariloche 8500, Río Negro, Argentina

⁴ Consejo Nacional de Investigaciones Científicas y Técnicas (CONICET), Buenos Aires, Argentina

Received: 3 December 2024 / Accepted: 19 January 2025

© The Author(s) 2025

Abstract This work compares simulated and measured neutron time-of-flight spectra for a cold neutron moderator with varying para-hydrogen concentrations (25%, 50%, 90% and 99.9%) embedded in a polyethylene thermal moderator. The primary neutrons are generated from the interaction of 45MeV protons with a tantalum target. The simulations were performed using several Monte Carlo codes (MCNP, PHITS, McStas, VITESS, and KDSOURCE) together with nuclear data from the ENDF/B-VII.1 and JENDL-5.0 libraries. The simulated primary neutron yields had deviations from experimental measurements ranging from 0.3 to 16% depending on the code and the nuclear data used. The neutron moderation in the para-hydrogen moderator coupled with a neutron guide was then modeled. The neutron time distribution was measured by a ³He detector at the end of the guide. Comparison with experimental data showed good agreement, with relative differences of less than 15%. For the 99.9% para-hydrogen concentration, simulations with JENDL-5.0 were in better agreement with the experimental data, while ENDF-B/VII.1 showed better agreement for the 25% para-hydrogen case. The analysis of the results obtained provides insights into the strengths and limitations of each Monte Carlo code and nuclear data library combination. The observed discrepancies were analyzed, and possible sources of error were also identified. The analytical procedure followed in this work will help to improve the accuracy and reliability of neutron cold moderator design.

1 Introduction

In recent decades, experimental techniques based on neutron scattering have become essential tools for studying condensed matter phenomena [1]. This type of experiments requires the usage of cold and thermal neutrons, as they have wavelengths comparable to the distances between the atoms of the samples and typical energies of their excitations. In particular, cold neutrons are especially useful for the study of large structures, low energy dynamics, and imaging applications [2]. As older research reactors face decommissioning, accelerator-driven neutron sources are emerging as promising alternatives to maintain and improve the supply of neutrons to the scientific community [3]. Several accelerator-based pulsed neutron sources are based on spallation reactions with proton beams of several GeV, such as the ISIS Neutron and Muon Source in the United Kingdom, the Spallation Neutron Source (SNS) in the USA, the Swiss Spallation Neutron Source (SINQ) in Switzerland, and the Japan Proton Accelerator Research Complex (J-PARC) in Japan, while the European Spallation Source (ESS) in Sweden is in the construction phase. On the other hand, High-Current Accelerator-driven Neutron Sources (HiCANS) have proton beams in the order of 3 to 100MeV [4]. In both of these kinds of pulsed sources, the fast neutrons (energies above 0.5MeV) produced in the target are slowed down into the thermal (energies below 0.5eV) and cold (energies below 10meV) energy ranges with suitable moderator systems.

The choice of the target, the reflector, and the moderator materials plays an important role in the performance of these sources, in order to shape the neutron pulse and maximize both the neutron yield at the target and the brilliance delivered to the neutron

^a e-mail: no.schmidt@fz-juelich.de (corresponding author)

^b e-mail: a.schwab@fz-juelich.de

^c e-mail: ji.li@fz-juelich.de

^d e-mail: u.ruecker@fz-juelich.de

^e e-mail: p.zakalek@fz-juelich.de

^f e-mail: e.mauerhofer@fz-juelich.de

^g e-mail: jdawidowski@cnea.gob.ar

^h e-mail: t.gutberlet@fz-juelich.de

instruments. Historically, solid methane has been used as a cold moderator due to its high hydrogen density and effective neutron slowing-down capabilities [5]. However, its susceptibility to radiation damage limits its use in high-power spallation sources, and therefore, liquid hydrogen has become an alternative [6].

The High Brilliance Neutron Source (HBS) project at Forschungszentrum Jülich GmbH [7] aims to develop a HiCANS for neutron scattering, analytics, and imaging. A fast neutron spectrum with an average energy of 0.5 MeV will be generated by the interaction of a 70 MeV proton beam of circa 80 mA peak current with a tantalum target. HBS will be provided with 3 different and independent target-moderator-reflector units that will operate at 24 Hz or 96 Hz to deliver individually tailored beam characteristics for each instrument [8]. For the cold neutron sources, both solid methane and liquid hydrogen are suggested to be used in very compact cryostats [9] to provide neutron instruments with beams with brightness values comparable to existing neutron sources in Europe [10].

To assess the performance of a compact para-hydrogen cryostat system as a cold neutron source in the frame of the technical design of the HBS project [7], a set of neutron time-of-flight spectrum measurements were performed [11] using the JULIC cyclotron of the Institute of Nuclear Physics (IKP) of the Forschungszentrum Jülich. The measurements were performed for different concentrations of para- and ortho-hydrogen. Also, Monte Carlo simulations have been carried out using several codes with different nuclear data libraries.

Monte Carlo codes like MCNP6 [12] or PHITS [13] can simulate high-energy nuclear physics processes, for which different physical models are used. Thus, in MCNP6, the Bertini [14], ISABEL [15], CEM03.03 [16], and INCL [17] models can be used, while in PHITS, the INCL, Bertini, JAM [18], and GEM [19] models are available. Furthermore, the default nuclear cross sections used by the two codes are different. Thus, MCNP6 uses the cross sections from ENDF/B-VII.1 [20], which does not include the tabulated values for the proton-induced reactions in ^{181}Ta , while PHITS offers by default the JENDL [21] database for cross sections, which in its version 5 [22] includes the tabulated data for proton-induced reactions. As for the models used to describe the scattering kernel $S(\alpha, \beta)$ of para- and ortho-hydrogen, in MCNP6 they are those developed by Keinert et al. [23], while in PHITS the liquid hydrogen models are the same as those used in JEFF-3.3 [24] developed by Granada et al. [25]. In general, the results obtained by these codes must be compared with experimental data, in order to validate the physical models and the nuclear cross sections used. Thus, the neutron spectra obtained by a para-hydrogen cold source were compared against Monte Carlo simulations in [26], and the total neutron yield for tantalum at different proton energies was validated in [27].

Considering that in most cases the transport of neutrons through neutron instruments does not take into account the moderation or the absorption of the neutrons with the materials composing the instrument, some codes were developed to perform the so-called ray tracing in a simpler way than Monte Carlo codes. In this line, McStas [28] and VITESS [29] are the most widely used, allowing to simulate neutron guides, ^3He detectors, and other components.

It is sometimes difficult to couple the output results of the simulations performed with Monte Carlo codes like MCNP6 for the full source geometry and the neutron instrument model used by the ray-tracing codes like McStas [30]. When coupling such simulations, it is also difficult to obtain adequate statistics in a reasonable computational time for positions far away from the source. Therefore, there are several variance reduction methods to increase the accuracy of the simulations. The open-source code KDSOURCE [31] is a recently developed alternative to solve this problem, because it checks the correlation between the variables of a given MCPL [32] particle list file using the kernel density estimation method and then gives the possibility to perturb the original files to obtain a new virtual source file with more particles than the original one.

In this work, we will show the cross-validation of simulations obtained by different Monte Carlo codes and nuclear data cross sections against experimental time-of-flight measurements.

2 Description of the experiments

Neutron spectra generated by a cold cryogenic moderator filled with different para- and ortho-hydrogen ratios at 20K were measured with the setup shown in Fig. 1. Fast neutrons were produced by the interaction of a 45 MeV proton beam with a Gaussian profile (14 mm full-width at half-maximum) with a tantalum target (80 mm diameter and 5 mm thickness). The width of the proton pulse was 200 μs , with frequencies of 12.5, 20, and 25 Hz. The neutrons were moderated in a polyethylene piece, which surrounds the cryogenic moderator (25 mm diameter and 100 mm length). The length of the cold moderator vessel was optimized and designed by means of Monte Carlo simulations to achieve the maximum intensity for a pure para-hydrogen composition. The contents of para-hydrogen studied were 25% (normal composition of H_2 at room temperature), 50%, 90%, and 99.9%. A 7 m long, ^{58}Ni -coated neutron guide with $30 \times 45 \text{ mm}^2$ cross section was placed at the end of a vacuum tube to transport the cold neutrons to a ^3He detector (gas pressure: 4 bar). The detector was connected to a time-of-flight counter board, and its time resolution was 200 bins of 0.5 ms each, corresponding to a 100 ms time-frame. The experimental setup is described in detail in [11].

The experimental results were normalized by the integral charge of protons measured for each case, i.e., mC or (mA·s). The measured neutron distribution at the ^3He detector as a function of the time-of-flight t [μs] was transformed into wavelength λ [Å] distributions with the equation

$$\lambda = \frac{t}{252.8L}, \quad (1)$$

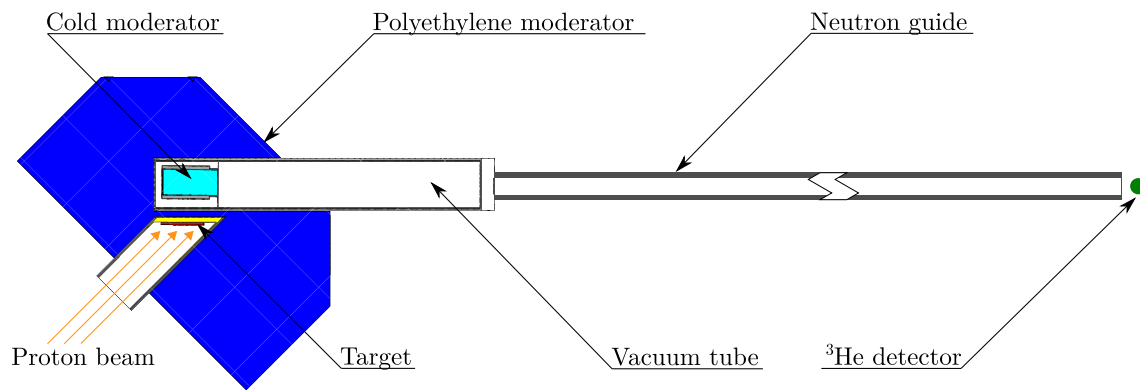
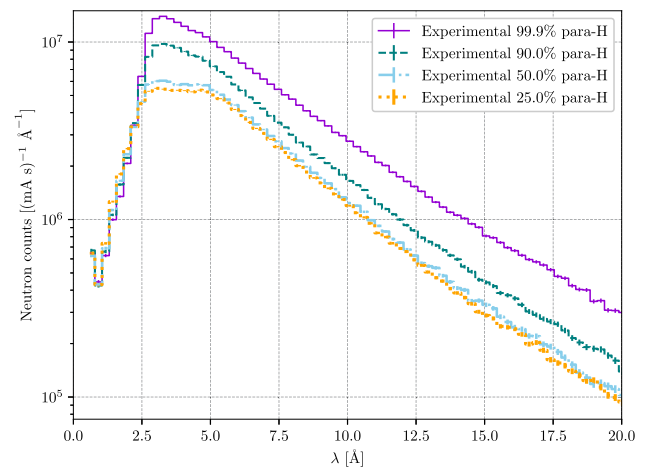


Fig. 1 Schematic model of the experimental setup used for the para-hydrogen time-of-flight measurements performed at the Forschungszentrum Jülich according to [11]. The dimensions of the different components are mentioned in the text. All the components are in relative scale, except the neutron guide

Fig. 2 Experimental results obtained for 99.9%, 90%, 50% and 25% para-H. The results are normalized by the integral charge of protons



where $L = 7.555(1)$ [m] is the time-of-flight distance between the cold moderator and the detector. The obtained experimental time-of-flight spectra for the different para-hydrogen concentrations are shown in Fig. 2.

3 Simulations

The simulation workflow is shown in Fig. 3. To facilitate the understanding of the process, the explanation of the workflow will be divided into five groups:

1. simulations of the primary fast neutron emission from the bare target,
2. simulations of the moderation of the fast neutrons within the polyethylene and para-hydrogen,
3. generation of virtual sources to increase the statistics,
4. simulations of the neutron transport within the neutron guide, and
5. simulation of the neutron detection at the ^3He detector.

All the results obtained from the simulations were also normalized by the number of primary protons in (mA·s). The uncertainties corresponding to the simulations are only those coming from the standard deviation of the mean value of the estimated variable distribution.

3.1 Primary fast neutron emission simulations

The neutron emission from interactions of 45MeV protons on a bare tantalum target was simulated using MCNP6 and PHITS 3.29. In MCNP6, 1×10^6 source particles were simulated with 1 CPU thread, requiring around 30 min of computational time. While in PHITS, 1×10^7 source particles were simulated with 8 CPU threads in about 8 min. The different physical models simulated with MCNP6 and PHITS are listed in Table 1, together with the integral neutron emission obtained with ENDF/B-VII.1 and JENDL-5.0/HE. The peak energies obtained for the different simulations are reported in Table 2.

Fig. 3 Workflow diagram indicating the methods used to simulate the experimental setup shown in Fig. 1

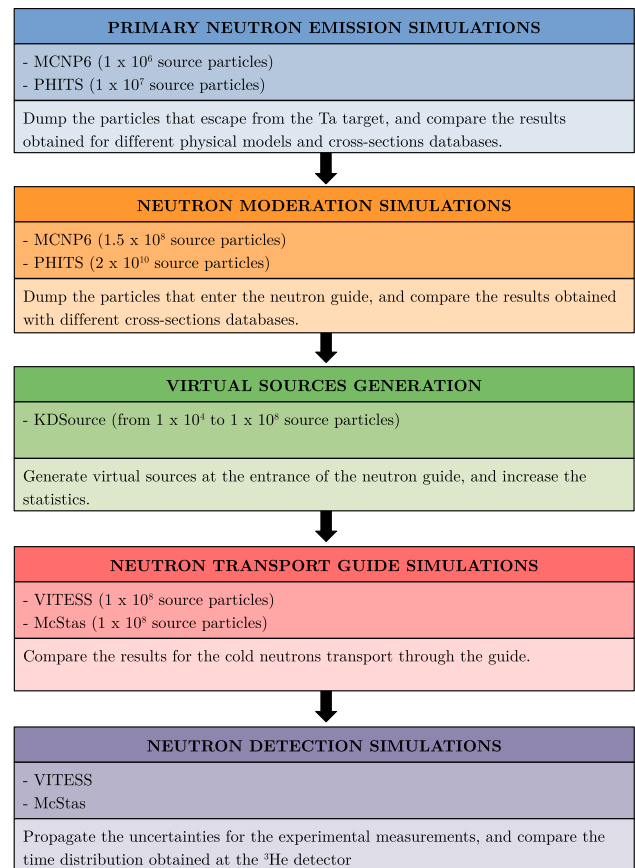


Table 1 Integral neutron emission values for a bare Ta target irradiated with 45MeV protons, obtained with MCNP6 and PHITS using different physical models and cross-section databases. Cases giving similar integral results and comparable neutron energy distributions were grouped into categories indicated by Roman numerals in brackets. The physical models indicated with * are the default for each code, while the one indicated with ** is the one recommended by the developers of the PHITS code

Code	Physical Model	ENDF/B-VII.1 [$\times 10^{14}$ (mA s) $^{-1}$]	JENDL-5.0/HE [$\times 10^{14}$ (mA s) $^{-1}$]
MCNP6	Bertini	3.70(2) (i)	2.86(1) (v)
	ISABEL	3.32(1) (ii)	2.86(1) (v)
	CEM03.03*	3.50(2) (iii)	2.86(1) (v)
	INCL/ABLA	3.92(2) (iv)	2.86(1) (v)
PHITS	INCL/GEM*	3.32(1) (vi)	2.86(1) (xii)
	INCL/GEM + e-mode**	3.33(1) (vi)	3.04(1) (vii)
	Bertini/GEM	3.92(2) (viii)	2.86(1) (xii)
	Bertini/GEM + e-mode	3.94(2) (viii)	3.60(2) (ix)
	Bertini/JAM	3.41(2) (x)	2.86(1) (xii)
	Bertini/JAM + e-mode	3.42(2) (x)	3.12(1) (xi)

Figure 4 shows the neutron energy distributions simulated with MCNP6 under different physical models. The simulation results highlight variations in the energy distribution shapes, particularly around the peak region and above 8 MeV. Additionally, there are differences in the lower-energy slopes of the distributions (below 1 MeV) across the models used. Since ENDF/B-VII.1 has no cross-sectional data for proton-induced reactions in ^{181}Ta , the differences in MCNP6 arise primarily from the physical model used.

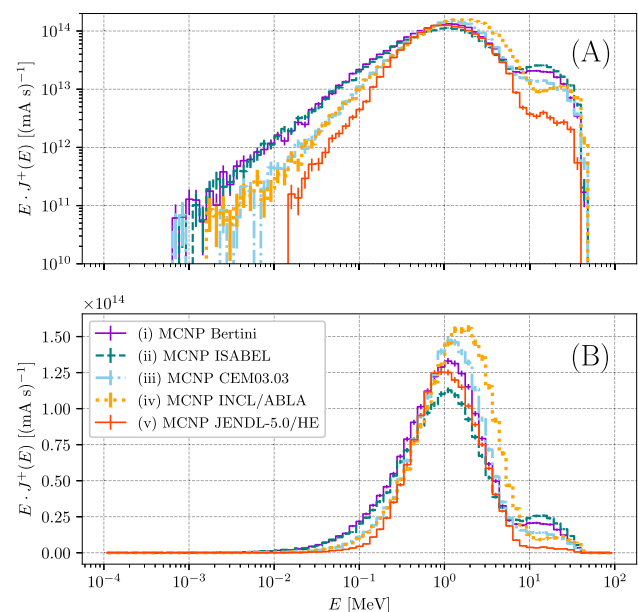
Figure 5 shows the neutron energy distributions obtained with PHITS under different physical models. For the simulations using JENDL-5.0/HE, the neutron spectra remain consistent across physical models, except when utilizing the event mode generator [33] recommended by the developers of PHITS. This consistency indicates that model choice in PHITS does not significantly alter results when JENDL-5.0/HE data are used, providing the same results in the distributions.

The combined results from MCNP6 and PHITS, shown in Fig. 6, compare the energy distributions under default modes in each code: CEM03.03 in MCNP6, INCL/GEM in PHITS, and the recommended INCL/GEM+e-mode in PHITS, as well as the results

Table 2 Peak energy of the spectra for a bare Ta target irradiated with 45MeV protons, obtained with MCNP6 and PHITS using different physical models and cross-section databases. Cases giving similar integral results and comparable neutron energy distributions were grouped into categories indicated by Roman numerals in brackets. The physical models indicated with * are the default for each code, while the one indicated with ** is the one recommended by the developers of the PHITS code

Code	Physical Model	ENDF/B-VII.1[MeV]	JENDL-5.0/HE[MeV]
MCNP6	Bertini	1.15(5) (i)	1.00(5) (v)
	ISABEL	1.10(5) (ii)	1.00(5) (v)
	CEM03.03*	1.20(5) (iii)	1.00(5) (v)
	INCL/ABLA	1.70(5) (iv)	1.00(5) (v)
PHITS	INCL/GEM*	1.25(5) (vi)	1.05(5) (xii)
	INCL/GEM + e-mode**	1.25(5) (vi)	1.25(5) (vii)
	Bertini/GEM	1.25(5) (viii)	1.05(5) (xii)
	Bertini/GEM + e-mode	1.25(5) (viii)	1.20(5) (ix)
	Bertini/JAM	1.25(5) (x)	1.05(5) (xii)
	Bertini/JAM + e-mode	1.25(5) (x)	1.25(5) (xi)

Fig. 4 Total neutron spectra for a bare Ta target irradiated with 45MeV protons, obtained with MCNP6 for the different cases listed in Table 1, in **A** logarithmic and **B** linear scale in ordinates



using JENDL–5.0/HE in both codes. JENDL–5.0/HE results are nearly identical between MCNP6 and PHITS as expected, but there are significant deviations, up to 37%, from other models in the total neutron emission. The general shape and peak differences underscore how each code handles energy distribution across these models. The discrepancies related to the different Monte Carlo codes, physical models, and cross-section databases were also observed in other works [34–37]; however, it was not the aim of this work to explain the origin of such discrepancies.

Finally, although direct comparisons to experimental data are affected by the absence of neutron energy distribution data specific to proton-induced reactions in ^{181}Ta , results obtained are in the same order of magnitude with the experimental results reported in [27] for a Ta target and 42 MeV protons, where the neutron yield was measured as $3.4(2) \times 10^{14} \text{ (mA s)}^{-1}$.

3.2 Neutron moderation simulations

Next, the complete geometry corresponding to Fig. 1 was modeled, again with MCNP6 (1.5×10^8 source particles, 113h simulation time) and PHITS 3.29 (2×10^{10} source particles, 60h simulation time). The different results for the physical models and the cross-section databases were compared. The difference between the number of source particles in both codes is due to the computational time elapsed for each simulation. All particles that crossed the surface corresponding to the beginning of the neutron guide were dumped into a particle list file. From these dump files, it is possible to analyze the outgoing angular current or brightness for a given surface as a function of the position \mathbf{r} , the direction $\hat{\mathbf{n}}$, the energy E , and the time t of the neutrons, $j^+(\mathbf{r}, \hat{\mathbf{n}}, E, t)$. When this outgoing

Fig. 5 Total neutron spectra for a bare Ta target irradiated with 45MeV protons, obtained with PHITS for the different cases listed in Table 1, in **A** logarithmic and **B** linear scale in ordinates

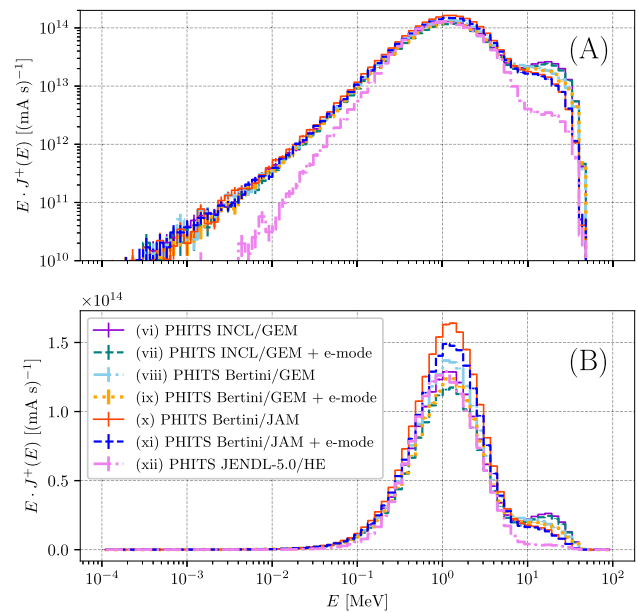
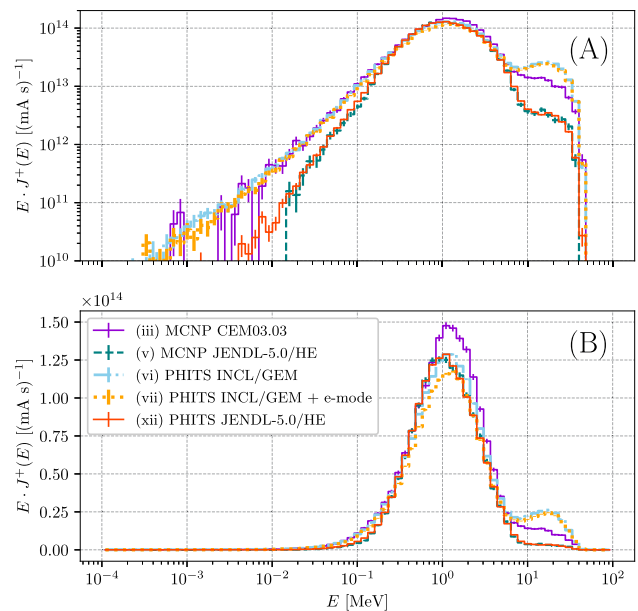


Fig. 6 Total neutron spectra for a bare Ta target irradiated with 45MeV protons, obtained with MCNP6 and PHITS along with different physical models and cross-section databases, in **A** logarithmic and **B** linear scale in ordinates



angular current is integrated over the range of solid angles in the outgoing directions, the outgoing current density $J^+(\mathbf{r}, E, t)$ is obtained.

The neutron angular current distribution as a function of the energy E and the polar angle from the flight direction ϑ at the entrance of the neutron guide for 99.9% para-H is shown in Fig. 7. The flight direction corresponding to the solid angle from the cold source to the neutron guide entrance is indicated with a black dashed-dotted line. For neutrons with energies above 10 MeV, the peak of the distribution is around a flight direction of 10° , corresponding to the solid angle from the Ta target to the entrance of the neutron guide. Some of the neutrons generated in the target had at least one scattering in the polyethylene and then crossed the neutron guide entrance with low probabilities with flight directions larger than 20° . For energies between 100 meV and 10 MeV, the distribution of the flight direction angle is uniform between 0° and 10° , and it is correlated with the moderating process of fast neutrons in the polyethylene moderator down to the thermal energy range. Then, for energies below 1eV, the flight direction angle shows a broadening over the full range because of the isotropic behavior of the thermalization of the neutrons in the polyethylene, with a peak in the distribution around 100 meV and 5° . However, a second peak can be distinguished around 10meV and flight directions below 5° , corresponding to the cold neutrons emitted from the cold source and feeding the neutron guide.

Fig. 7 Neutron angular current j^+ as a function of the energy E and flight direction angle ϑ at the entrance of the neutron guide for 99.9% para-H, obtained with PHITS using JENDL-5.0/HE. The collimation angle corresponding to the solid angle between the cold source and the entrance of the neutron guide is indicated with a black dashed-dotted line

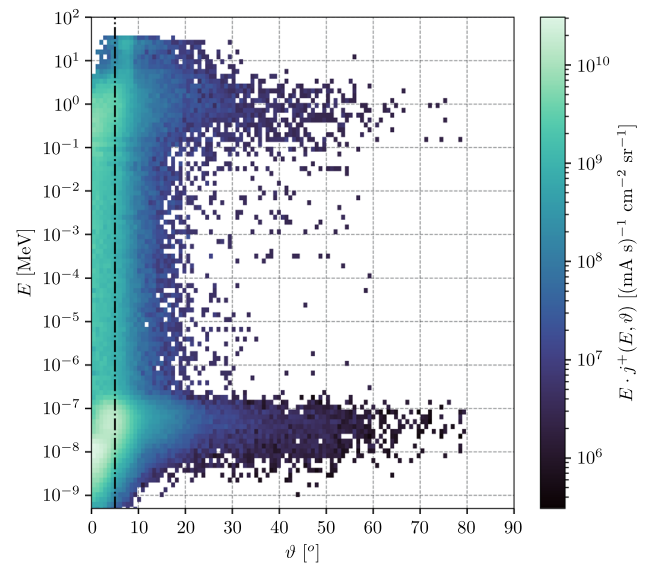
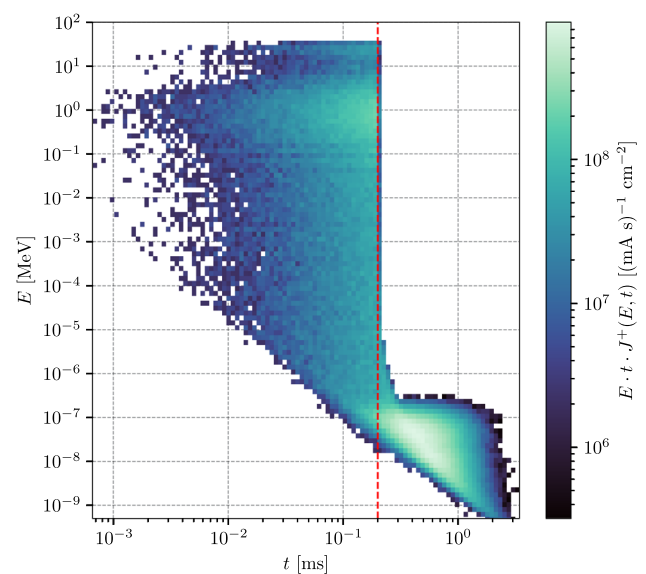


Fig. 8 Neutron current $J^+(E, t)$ at the entrance of the neutron guide for 99.9% para-H, obtained with PHITS using JENDL-5.0/HE. The proton pulse width is indicated with a red dashed line



The neutron current distribution as a function of the energy E and the time t at the entrance of the neutron guide for 99.9% para-H is shown in Fig. 8. These results are obtained after integrating the distributions from Fig. 7 over all the flight directions, i.e., a solid angle of 2π . The proton pulse width of 200 μs is indicated with a red dashed line.

The comparison of the neutron spectra obtained at the entrance of the neutron guide with the different codes is shown in Fig. 9. These results are obtained after integrating the distributions from Fig. 8 over time. For the fast neutrons, the discrepancies were already observed for the bare target simulations in Fig. 6, and the differences are less than 20% for the whole energy spectra and less than 15% for energies below 0.5 eV. Considering the dependence on the flight direction and the energy range of the neutrons, the integral neutron current values obtained at the entrance of the neutron guide for different angular and energy domains using the different codes and physical models are indicated in Table 3. The results between MCNP6 and PHITS are close to each other, but it was possible to run more particles in the same time frame with PHITS. Therefore, the results obtained with PHITS using the different cross sections will be used from now on.

3.3 Virtual sources generation

For each simulation, only about 1×10^4 neutrons crossed the surface corresponding to the beginning of the neutron guide, and only about 7×10^2 of them arrived at the ^3He detector. To avoid the long-time simulation needed by increasing the number of source particles to achieve reasonable counting statistics at the ^3He detector, the open-source code KDSources was used to generate new

Fig. 9 Neutron spectra at the entrance of the neutron guide for 99.9% para-H, obtained with MCNP6 and PHITS along with different physical models and cross-section databases. The ratio between the results with PHITS and MCNP are shown for comparison in the lower frame

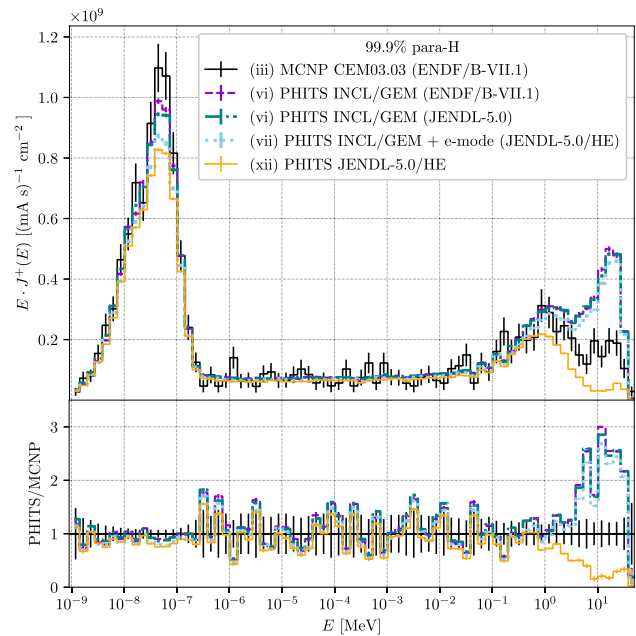
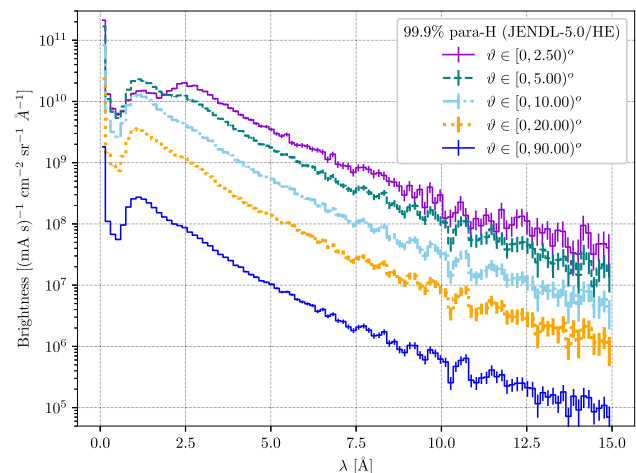


Table 3 Neutron current values at the entrance of the neutron guide for 99.9% para-H, obtained with MCNP6 and PHITS using different physical models and cross-section databases. The integral of the angular current was performed for different ranges of energy E and polar angle from the flight direction ϑ of the neutrons. The Roman numbers in brackets in the first column are the groups introduced in Tables 1 and 2

Code, physical model, and cross sections	Neutron current [$\times 10^9$ (mA s) $^{-1}$ cm $^{-2}$]		
	$E \in [0, 45]$ MeV $\vartheta \in [0, 90]^\circ$	$E \in [0, 0.5]$ eV $\vartheta \in [0, 90]^\circ$	$E \in [0, 0.5]$ eV $\vartheta \in [0, 5]^\circ$
(iii) MCNP6 CEM03.03 (ENDF/B-VII.1)	4.8(1)	2.66(7)	1.33(5)
(vi) PHITS INCL/GEM (ENDF/B-VII.1)	5.17(1)	2.516(8)	1.247(6)
(vi) PHITS INCL/GEM (JENDL-5.0)	5.15(1)	2.514(6)	1.252(4)
(vii) PHITS INCL/GEM + e-mode (JENDL-5.0/HE)	4.73(1)	2.302(7)	1.146(5)
(xii) PHITS JENDL-5.0/HE	3.744(8)	2.216(6)	1.129(4)

Fig. 10 Neutron brightness at the entrance of the neutron guide for 99.9% para-H, obtained with PHITS using JENDL-5.0/HE



virtual sources of 1×10^8 neutrons at this point. The distributions obtained with the new virtual sources are compared after the transport through the neutron guide, as shown in the next section.

Fig. 11 Neutron brightness at the exit of the neutron guide for 99.9% para-H, obtained with McStas and VITESS

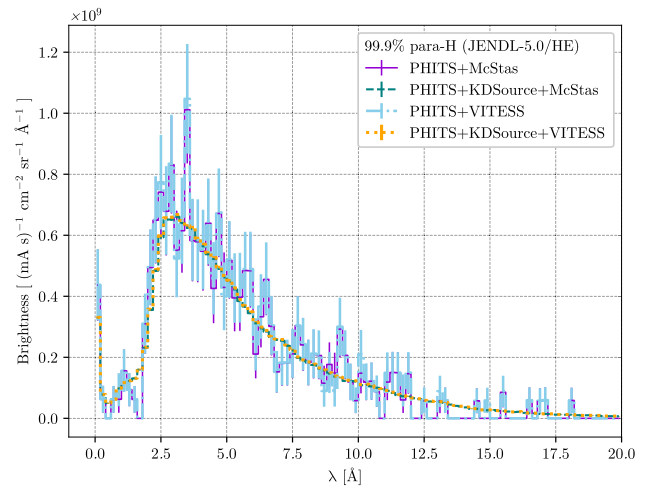
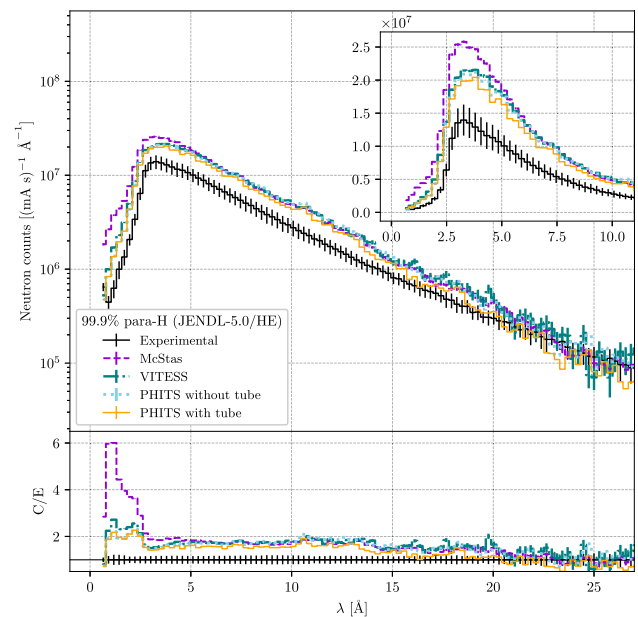


Fig. 12 Comparison between the experimental spectrum and the simulations using McStas, VITESS, and PHITS for 99.9% para-H, using JENDL-5.0/HE. The inset shows a zoom of the same spectra on a linear scale in ordinates. The ratio between the calculations and the experimental values are shown for comparison in the lower frame



3.4 Neutron guide simulations

After the generation of the virtual sources, the simulations of the transport through the neutron guide have been performed using the ray-tracing codes VITESS and McStas. The reflectivity R of the guide, as a function of scattering vector length Q , was modeled for both codes [38, 39] as:

$$R(Q) = \begin{cases} R_0 & \text{if } Q \leq Q_c \\ \frac{1}{2} R_0 [1 - \alpha(Q - Q_c)] \left[1 - \tanh \left(\frac{Q - mQ_c}{W} \right) \right] & \text{if } Q > Q_c, \end{cases} \quad (2)$$

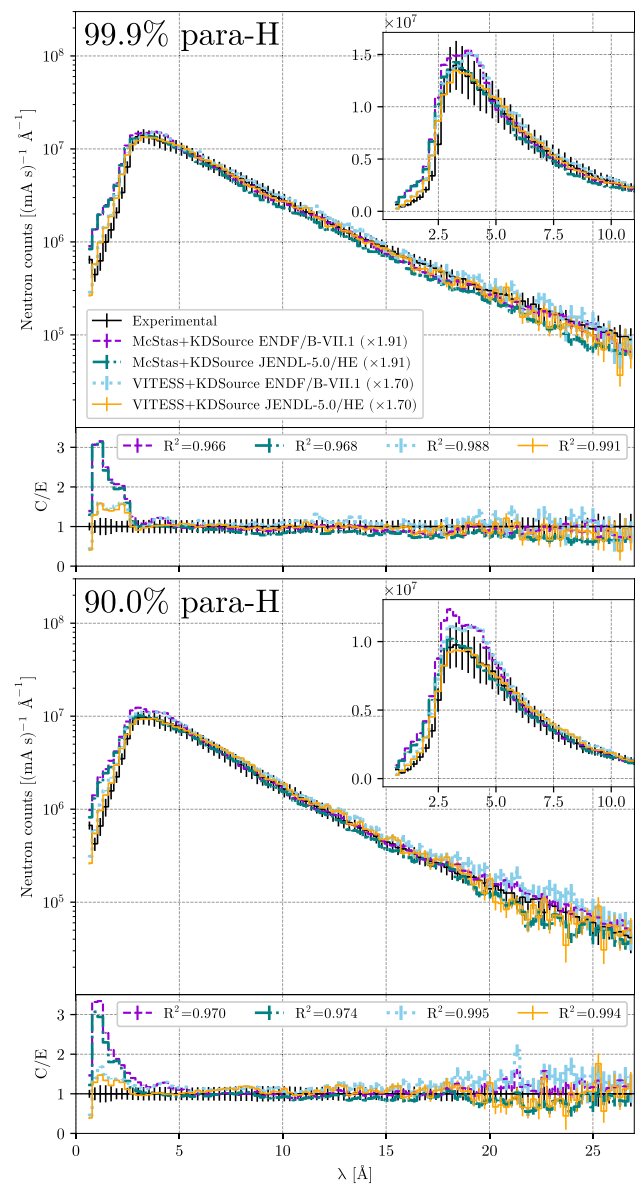
where $Q_c = 0.0217 \text{ \AA}^{-1}$ is the critical scattering vector length, $m = 1.16$ is the m -value of the guide, $R_0 = 0.99$ is the reflectivity for $Q < Q_c$, $W = 0$ is the width of the cut-off from $Q = Q_c$ to $Q = mQ_c$, and $\alpha = 0$ is the slope of the cut-off.

At the end of the neutron guide, the neutrons were again dumped into a particle list file to compare the performance of the ray-tracing codes. The results obtained with the Monte Carlo and the ray-tracing codes were coupled by calculating the neutron intensity at the entrance of the neutron guide for a specific volume of the phase space (\mathbf{r} , $\hat{\mathbf{n}}$, E , t), and then equating these results.

The neutron brightness at the entrance of the neutron guide is shown in Fig. 10. Following the dependence between the energy and the flight direction angle of the neutrons (see Fig. 7), the brightness was calculated for angles of 2.5° , 5° , 10° , 20° , and 90° . The cold neutron peak around 2.5 \AA is only distinguishable for flight directions below 5° .

The results for the neutron brightness at the end of the neutron guide after the transport simulation with VITESS and McStas are shown in Fig. 11, and no differences were found between the results. The results with and without using the virtual sources

Fig. 13 Comparison between the experimental results and the simulations using McStas and VITESS for 99.9% and 90% para-H, using different cross-section databases (ENDF/B-VII.1 and JENDL-5.0/HE). For each, an inset shows a zoom of the same spectra on a linear scale in ordinates, and the ratio between the calculations and the experimental values C/E is shown in the lower frame of the plots



generated with KDSOURCE matched against each other, showing how the use of KDSOURCE improves the statistics while reducing the total time required for the simulations¹.

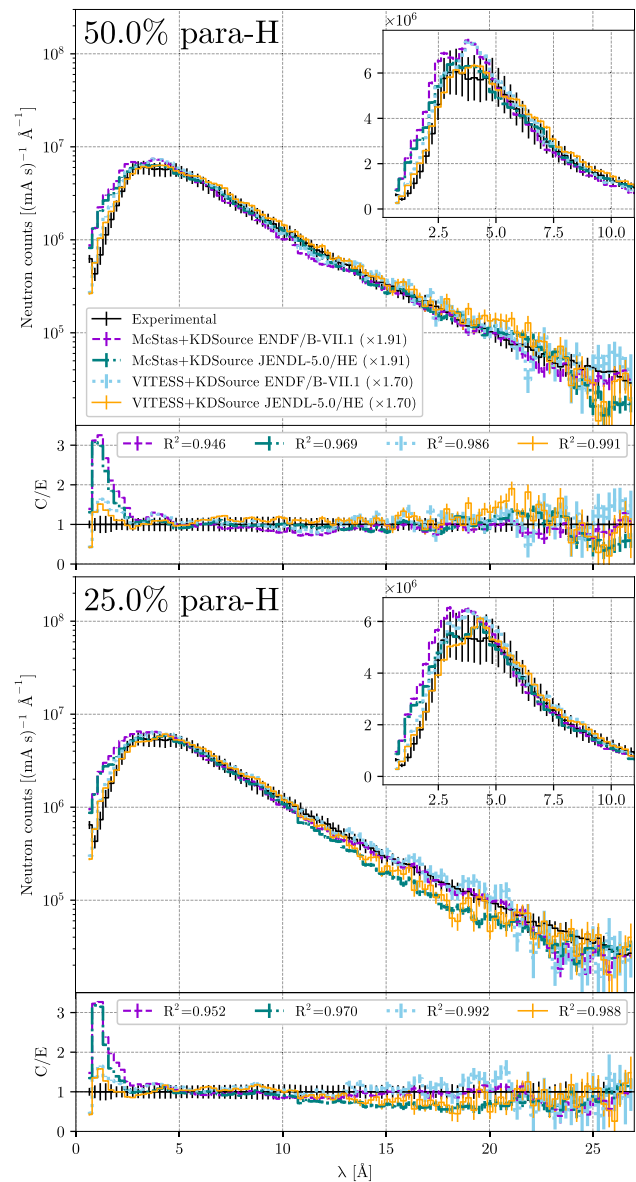
3.5 Detector simulations

For the experimental results, the following uncertainties were considered: the ^3He pressure P ($4 \text{ bar} \pm 10\%$), the m -value of the guide ($1.16 \pm 10\%$), the reflectivity of the guide R_0 (0.9, 0.99, and 0.999), and the orientation of the guide with respect to the cold source ($\pm 0.5^\circ$). The different combinations of all these possible systematic uncertainties ($3^4 = 81$ cases) were simulated with VITESS to calculate the standard deviations from the base case ($P = 4 \text{ bar}$, $m = 1.16$, $R = 0.99$). These standard deviations were propagated to each bin of the experimental values, together with the corresponding Poisson standard deviation.

The neutron counts for the wavelength distributions obtained with the different codes inside the ^3He detector are shown in Fig. 12. As mentioned in Sect. 2, these results were calculated from the time distributions at the detectors and then transformed using Equation (1). The results obtained are different for both McStas and VITESS codes. This can be explained by checking how the

¹ The simulations with PHITS of 2×10^{10} source particles were 60h long, and only 1×10^4 neutrons crossed-in the entrance of the neutron guide. To obtain 1×10^8 neutrons at this position, the PHITS simulation would have been 6×10^9 h long, while the generation of the virtual sources with KDSOURCE took less than 10m for each dump file.

Fig. 14 Comparison between the experimental results and the simulations using McStas and VITESS for 50% and 25% para-H, using different cross-section databases (ENDF/B-VII.1 and JENDL-5.0/HE). For each, an inset shows a zoom of the same spectra on a linear scale in ordinates, and the ratio between the calculations and the experimental values C/E is shown in the lower frame of the plots



detector component in VITESS and the `Monitor_nD` component in McStas implement the efficiency calculation². The ^3He detector was also modeled and simulated in PHITS to cross-check the results, using the dump file at the end of the neutron guide as an external source, with and without the stainless steel tube housing (0.5mm thickness) of the detector. This was done because the tube housing is not modeled in McStas and VITESS, but it was desired to check how the presence of the stainless steel affects the detector efficiency. The results obtained with PHITS are closer to the ones obtained with VITESS.

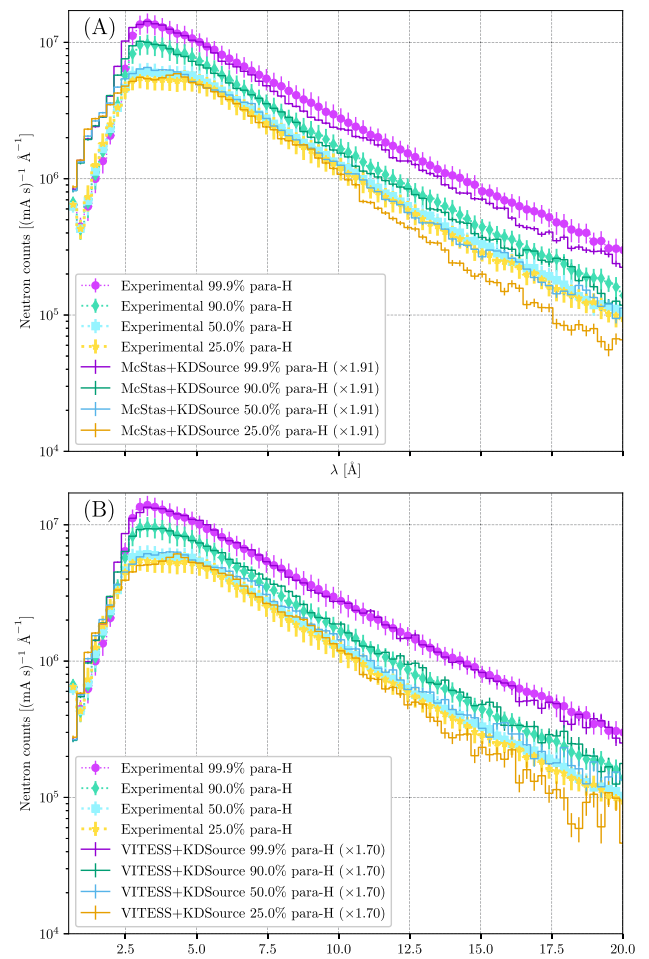
For all the simulated cases, the intensity of the neutron wavelength distribution inside the ^3He detector is higher than the experimental values. This can be attributed to uncertainties coming from the measurement of the proton current and configuration of the detection electronic chain (signal amplification, pulse discrimination, noise rejection, dead time). Therefore, this systematic error should be independent of the para-hydrogen measurements. To renormalize the results and avoid the use of “arbitrary units” like has been done in [26], the simulated values y_{sim} for each time bin t were linearly fitted against the experimental data y_{exp} with the following expression:

$$y_{\text{sim}(i,j,k)}(t) = b_{(i,j,k)} + m_{(i,j,k)} \cdot y_{\text{exp}(i,j,k)}(t), \quad (3)$$

where m and b are the slope and the y-intercept, respectively. This fitting has been done for each combination of ray-tracing code i (McStas, VITESS), cross-sections database j (ENDF/B-VII.1, JENDL-5.0/HE), and para-hydrogen concentration k (25%, 50%,

² The ^3He detector can also be modeled with the new `UNION` components in McStas [40]. However, this was not done in this work to keep the simulations as simple as possible using the default monitors and detectors available in VITESS and McStas.

Fig. 15 Comparison between the experimental and simulated results for 99.9%, 90%, 50%, and 25% para-H, using **A** VITESS and **B** McStas with the JENDL-5.0/HE cross-sections database



90%, 99.9%). The average of the fitted slopes $m_{(i,j,k)}$ over all the para-hydrogen concentrations for each ray-tracing code was calculated, using the JENDL-5.0/HE cross-sections database as reference:

$$\langle m \rangle_i = \frac{\sum_k m_{(i,j=JENDL-5.0/HE,k)}}{4}. \quad (4)$$

Thus, two values were obtained ($\langle m \rangle_{VITESS} = 1.7$ and $\langle m \rangle_{McStas} = 1.91$), which were used as normalization factors for VITESS and McStas, respectively.

The comparison of the results obtained with the simulations against the experimental data for 99.9%, 90%, 50%, and 25% para-H is shown in Figs. 13 and 14. The distributions obtained with McStas and VITESS are multiplied by the normalization factors as explained before. For all the cases, the results obtained with VITESS give a better agreement along the full wavelength range, and the results obtained with McStas have some discrepancies for wavelengths below 2.5 Å. For wavelengths above 2.5 Å, the differences between the experimental data and the simulations are less than 15% in most of the cases.

3.6 Discussion

A summary of the comparison between the experimental data and the simulations obtained for all the different para-H ratios is shown in Fig. 15. As it was proven and discussed in [26], this work together with [11] shows that the neutron wavelength distribution has a strong dependence on the para-H concentration. The experiments proved that, for a moderator thickness of 10cm, the best performance is obtained for pure para-H compared to the other para-H concentrations.

For almost all the different para-H concentrations, the results using JENDL-5.0/HE are in better agreement with the experimental values than those obtained with ENDF/B-VII.1. The only case when the tendency seems to be the opposite is for 25% para-H, and this might be attributed to an error in the production of the ortho-H scattering kernel in the JENDL-5.0/HE database. After a discussion with the authors of Ref. [41], we concluded that it would be possible to generate new cross-sections for ortho-H and compare the results. The reader should notice that the use of ortho-H is not optimal for the generation of cold neutrons [11] [26]. Therefore, the neutron physics community is focused on generating the best description of the para-H scattering kernels.

4 Conclusions

In this work, the authors intended to provide a comparative analysis of neutron time-of-flight results obtained from different simulations of an experimental cold neutron moderator with different para- and ortho-hydrogen concentrations (25%, 50%, 90%, and 99.9%). The study used several Monte Carlo codes, including MCNP6, PHITS, McStas, VITESS, and KDSOURCE, with nuclear data from the ENDF/B-VII.1 and JENDL-5.0 libraries.

The neutron yield for 45 MeV protons irradiating into a Ta target was calculated with MCNP6 and PHITS, using different physical models and cross-section databases. The values obtained for the integral neutron yield were in the same order of magnitude as those reported in [27], but no conclusions could be drawn regarding the energy distribution of the neutrons due to the lack of experimental data.

The experimental setup with the polyethylene moderator and the para-H cryostat was further modeled with MCNP6 and PHITS. For the different physical models, the results showed relative differences of about 30% over the whole energy range, which decreased to 15% for the cold and thermal neutrons with a solid angle divergence equivalent to 5°. The choice of cross-section database did not lead to significant differences.

To increase the statistics at the end of the neutron guide and reduce the computational simulation time, new virtual sources were generated at the neutron guide entrance with the open-source code KDSOURCE. The results obtained with these virtual sources showed a good agreement with the results obtained without using KDSOURCE, and the simulations of neutron transport through the guide using VITESS and McStas with these new virtual sources showed no differences at the guide's end. However, discrepancies emerged between the two codes at the ^3He detector, particularly for neutron wavelengths below 2.5 Å. A systematic error was identified in comparison with experimental data; therefore, a normalization factor was calculated for absolute comparison. With this normalization, simulation results were within 15% of experimental values.

The results obtained with JENDL-5.0/HE for pure para-H showed a better agreement with experimental data than those using ENDF-B/VII.1. On the other hand, the agreement seemed slightly better with ENDF/B-VII.1 for 25% para-H (normal ratio). These differences may be due to an error in the production of ortho-H cross sections in JENDL-5.0/HE.

Acknowledgements The authors would like to thank Dr. José Ignacio Márquez Damián (ESS, Sweden), Dr. Rolando Granada (CAB, Argentina), Dr. Douglas DiJulio (ESS, Sweden), Dr. Klaus Lieutenant (JCNS-2, Germany), and Dr. Jörg Voigt (JCNS-2, Germany) for their ideas and helpful advice.

Author contributions N.S. Schmidt contributed to methodology, software, validation, and writing—original draft. A. Schwab contributed to methodology and investigation. J. Li contributed to software and writing—reviewing and editing. U. Rücker contributed to methodology, investigation, and writing—reviewing and editing. P. Zakalek contributed to methodology, investigation, and writing—reviewing and editing. E. Mauerhofer contributed to conceptualization, writing—reviewing and editing, and supervision. J. Dawidowski contributed to conceptualization, writing—reviewing and editing, and supervision. T. Gutberlet contributed to writing—reviewing and editing, project administration, and funding.

Funding Open Access funding enabled and organized by Projekt DEAL. This project has received funding from Forschungszentrum Jülich (“Tasso Springer Fellowship Program”), CONICET (PIP 11220200102121CO), and ANPCYT (PICT-2019-02665).

Data Availability Statement The manuscript has associated data in a data repository. All metadata presented in this article are stored at Jülich Centre for Neutron Science, Forschungszentrum Jülich GmbH. Datasets generated during the current study are available from the corresponding author on reasonable request.

Declarations

Conflict of interest The authors declare that they have no known competing financial interests or personal relationships that could have appeared to influence the work reported in this paper.

Consent to participate Not applicable.

Ethics approval Not applicable.

Open Access This article is licensed under a Creative Commons Attribution 4.0 International License, which permits use, sharing, adaptation, distribution and reproduction in any medium or format, as long as you give appropriate credit to the original author(s) and the source, provide a link to the Creative Commons licence, and indicate if changes were made. The images or other third party material in this article are included in the article's Creative Commons licence, unless indicated otherwise in a credit line to the material. If material is not included in the article's Creative Commons licence and your intended use is not permitted by statutory regulation or exceeds the permitted use, you will need to obtain permission directly from the copyright holder. To view a copy of this licence, visit <http://creativecommons.org/licenses/by/4.0/>.

References

1. Neutron Science in Europe. League of advanced European Neutron Sources (LENS) (2022)
2. Cold Neutron Sources: Practical Considerations and Modern Research. TECDOC Series, vol. 2025. International Atomic Energy Agency (IAEA), Vienna (2023). <https://www.iaea.org/publications/15409/cold-neutron-sources-practical-considerations-and-modern-research>

3. T. Brückel, T. Gutberlet, S. Schmidt, C. Alba-Simionesco, F. Ott, A. Menelle, Low energy accelerator-driven neutron facilities—A prospect for a brighter future for research with neutrons. *Neutron News* **31**(2–4), 13–18 (2020)
4. A. Lehrach, J. Baggemann, Y. Bessler, T. Brückel, O. Felden, T. Gutberlet, R. Hanslik, J. Li, E. Mauerhofer, U. Rücker, et al. Establishing a new class of high-current accelerator-driven neutron sources with the HBS Project. *Proc. IPAC'24*, 129–132
5. M.H. Parajon, E. Abad, F. Bermejo, A review of the cold neutron moderator materials: neutronic performance and radiation effects. *Phys. Procedia* **60**, 74–82 (2014)
6. Y. Kiyanagi, M. Ooi, H. Ogawa, M. Furusaka, Development of hydrogen cold moderator systems for a spallation neutron source. *J. Neutron Res* **11**(1–2), 3–11 (2003)
7. T. Brückel, T. Gutberlet, Opportunities for Research with Neutrons at the Next Generation Facility HBS - Overview of the High Brilliance Neutron Source (HBS) Technical Design Report. Forschungszentrum Jülich GmbH, Jülich. dx.doi.org/10.34734/FZJ-2023-03726 (2023)
8. J. Voigt, K. Lieutenant, An Instrument Suite for the HBS. In: *EPJ Web of Conferences*, vol. 298, p. 01004 (2024). EDP Sciences
9. U. Rücker, I. Pechenizkiy, J. Li, E. Vezhlev, P. Zakalek, J. Voigt, T. Gutberlet, Brückel, T.: Thermal moderator-reflector assembly for HBS. In: *EPJ Web of Conferences*, vol. 298, p. 05008. EDP Sciences (2024)
10. J. Baggemann, E. Mauerhofer, U. Rücker, P. Zakalek, T. Gutberlet, T. Brückel, Technical Design Report HBS Volume 2 – Target Stations and Moderators. Forschungszentrum Jülich GmbH, Jülich. dx.doi.org/10.34734/FZJ-2023-03723 (2023)
11. A. Schwab, S. Eisenhut, J. Baggemann, J. Li, K. Lieutenant, U. Rücker, N. Schmidt, M. Strothmann, P. Zakalek, O. Felden, T. Gutberlet, T. Brückel, Neutron time of flight measurements for different ortho- to para-hydrogen ratios using a novel cryostat. Under preparation
12. T. Goorley, M. James, T. Booth, F. Brown, J. Bull, L. Cox, J. Durkee, J. Elson, M. Fensin, R. Forster et al., Initial MCNP6 release overview. *Nuclear technol.* **180**(3), 298–315 (2012)
13. T. Sato, Y. Iwamoto, S. Hashimoto, T. Ogawa, T. Furuta, S.-I. Abe, T. Kai, Y. Matsuya, N. Matsuda, Y. Hirata, et al. Recent improvements of the particle and heavy ion transport code system—PHITS version 3.33. *Journal of Nuclear Science and Technology* **61**(1), 127–135 (2024)
14. H.W. Bertini, Intranuclear-Cascade Calculation of the Secondary Nucleon Spectra from Nucleon-Nucleus Interactions in the Energy Range 340 to 2900 MeV and Comparisons with Experiment. *Phys. Rev.* **188**, 1711–1730 <https://doi.org/10.1103/PhysRev.188.1711> (1969)
15. Z. Fraenkel, A. Gavron, ISABEL EVA PACE-2, Evaporation Model with Intranuclear Cascade Input (1998)
16. L.M. Kerby, S.G. Mashnik, A.J. Sierk, Comparison of Expanded Preequilibrium CEM Model with CEM03.03 and Experimental Data, FY2013 (2013) <https://doi.org/10.2172/1107982>
17. A. Boudard, J. Cugnon, J.-C. David, S. Leray, D. Mancusi, New potentialities of the Liège intranuclear cascade model for reactions induced by nucleons and light charged particles. *Phys. Rev. C* **87**, 014606 (2013) <https://doi.org/10.1103/PhysRevC.87.014606>
18. Y. Nara, N. Otuka, A. Ohnishi, K. Niita, S. Chiba, Relativistic nuclear collisions at 10 A GeV energies from p+ Be to Au+ Au with the hadronic cascade model. *Phys. Review C* **61**(2), 024901 (1999)
19. S. Furihata, K. Niita, S.-i. Meigo, Y. Ikeda, F. Maekawa, The GEM code. A simulation program for the evaporation and the fission process of an excited nucleus. Technical report, Japan Atomic Energy Research Inst. (2001)
20. M.B. Chadwick, M. Herman, P. Obložinský, M.E. Dunn, Y. Danon, A. Kahler, D.L. Smith, B. Pritychenko, G. Arbanas, R. Arcilla, et al. ENDF/B-VII. 1 nuclear data for science and technology: cross sections, covariances, fission product yields and decay data. *Nuclear data sheets* **112**(12), 2887–2996 (2011)
21. K. Shibata, O. Iwamoto, T. Nakagawa, N. Iwamoto, A. Ichihara, S. Kunieda, S. Chiba, K. Furutaka, N. Otuka, T. Ohsawa, et al. JENDL-4.0: a new library for nuclear science and engineering. *Journal of Nuclear Science and Technology* **48**(1), 1–30 (2011)
22. O. Iwamoto, N. Iwamoto, S. Kunieda, F. Minato, S. Nakayama, Y. Abe, K. Tsubakihara, S. Okumura, C. Ishizuka, T. Yoshida et al., Japanese evaluated nuclear data library version 5: JENDL-5. *J. Nuclear Sci. Technol.* **60**(1), 1–60 (2023)
23. J. Keinert, J. Sax, Investigation of neutron scattering dynamics in liquid hydrogen and deuterium for cold neutron sources/Untersuchung der Neutronenstreuung in flüssigem Wasserstoff und Deuterium für Quellen kalter Neutronen: Dedicated to Professor Dieter Emendörfer, Stuttgart, on his 60th birthday. *Kerntechnik* **51**(1), 19–23 (1987)
24. A.J. Plompen, O. Cabellos, C. De Saint Jean, M. Fleming, A. Algora, M. Angelone, P. Archier, E. Bauge, O. Bersillon, A. Blokhin, et al.: The joint evaluated fission and fusion nuclear data library, JEFF-3.3. *The European Physical Journal A* **56**, 1–108 (2020)
25. J. Granada, V. Gillette, A new thermal neutron scattering kernel for liquid hydrogen. *Phys. B: Condensed Matter* **348**(1–4), 6–14 (2004)
26. M. Ooi, H. Ogawa, T. Kamiyama, Y. Kiyanagi, Experimental studies of the effect of the ortho/para ratio on the neutronic performance of a liquid hydrogen moderator for a pulsed neutron source. *Nuclear Instruments and Methods in Phys. Res. Section A: Accelerators, Spectrometers, Detectors and Associated Equipment* **659**(1), 61–68 (2011)
27. M. Rimmler, J. Baggemann, S. Böhm, P.-E. Doege, O. Felden, N.-O. Fröhlich, R. Gebel, J. Li, J. Li, E. Mauerhofer et al., Determination of the neutron yield of Be, V and Ta targets irradiated with protons (22–42 MeV) by means of prompt gamma neutron activation analysis. *Nuclear Instruments and Methods in Phys. Res. Section A: Accelerators, Spectrometers, Detectors and Associated Equipment* **990**, 164989 (2021)
28. K. Lefmann, K. Nielsen, McStas, a general software package for neutron ray-tracing simulations. *Neutron news* **10**(3), 20–23 (1999)
29. C. Zendler, K. Lieutenant, D. Nekrasov, M. Fromme, VITESS 3—virtual instrumentation tool for the European spallation source. In: *Journal of Physics: Conference Series*, vol. 528, p. 012036 (2014). IOP Publishing
30. E. Klinkby, B. Lauritzen, E. Nonbøl, P.K. Willendrup, U. Filges, M. Wohlmuther, F.X. Gallmeier, Interfacing MCNPX and McStas for simulation of neutron transport. *Nuclear Instruments and Methods in Phys. Res. Section A: Accelerators, Spectrometers, Detectors and Associated Equipment* **700**, 106–110 (2013)
31. N.S. Schmidt, O.I. Abbate, Z.M. Prieto, J.I. Robledo, J.M. Damián, A.A. Marquez, J. Dawidowski, KDSOURCE, a tool for the generation of Monte Carlo particle sources using kernel density estimation. *Annals of Nuclear Energy* **177**, 1093010930109309 (2022)
32. T. Kittelmann, E. Klinkby, E.B. Knudsen, P. Willendrup, X.-X. Cai, K. Kanaki, Monte Carlo particle lists: MCPL. *Comp. Phys. Communications* **218**, 17–42 (2017)
33. Y. Iwamoto, K. Niita, Y. Sakamoto, T. Sato, N. Matsuda, Validation of the event generator mode in the PHITS code and its application. In: *International Conference on Nuclear Data for Science and Technology*, pp. 945–948 (2007). EDP Sciences
34. J. Oh, H.-S. Lee, S. Park, M. Kim, S. Hong, S. Ko, W.-K. Cho, Comparison of the FLUKA, MCNPX, and PHITS codes in yield calculation of secondary particles produced by intermediate energy proton beam. *Carbon* **3**(5.83), 11 (2011)
35. Z.-Y. Yang, P.-E. Tsai, S.-C. Lee, Y.-C. Liu, C.-C. Chen, T. Sato, R.-J. Sheu, Inter-comparison of dose distributions calculated by FLUKA, GEANT4, MCNP, and PHITS for proton therapy. In: *EPJ Web of Conferences*, vol. 153, p. 04011 (2017). EDP Sciences
36. T. Nishitani, S. Yoshihashi, K. Kumagai, K. Kondo, A. Uritani, Benchmark calculation of d-li thick target neutron yield by jendl/deu-2020 for ifmif and similar facilities. *Plasma and Fusion Res.* **16**, 1405104–1405104 (2021)
37. Y. Çelik, A. Stankovskiy, H. Iwamoto, Y. Iwamoto, G. Eynde, Built-in physics models and proton-induced nuclear data validation using MCNP, PHITS, and FLUKA-Impact on the shielding design for proton accelerator facilities. *Annals of Nuclear Energy* **212**, 111048 (2025)

38. C. Zendler, K. Lieutenant, D. Nekrassov, M. Fromme, Vitess 3—virtual instrumentation tool for the european spallation source. In: *Journal of Physics: Conference Series*, vol. 528, p. 012036 (2014). IOP Publishing
39. P.K. Willendrup, K. Lefmann, McStas (ii): An overview of components, their use, and advice for user contributions. *J. Neutron Res.* **23**(1), 7–27 (2021)
40. M. Bertelsen, P. Willendrup, T.R. Nielsen, K. Lefmann, Simulation of complex neutron detectors using new features in the McStas Union components. Talk presented at the European Conference on Neutron Scattering (2023)
41. D.D. DiJulio, J.I.M. Damian, G. Muhrer, Generation of thermal neutron scattering libraries for liquid para-hydrogen and ortho-deuterium using ring-polymer molecular dynamics. In: *EPJ Web of Conferences*, vol. 284, p. 17006 (2023). EDP Sciences